*Nano Research* 2015, 8(1): 184–192
DOI 10.1007/s12274-014-0609-6
**Research Article**
ISSN 1998-0124
CN 11-5974/O4

# Ice-templated preparation and sodium storage of ultrasmall $SnO_2$ nanoparticles embedded in three-dimensional graphene

Longkai Pei, Qi Jin, Zhiqiang Zhu, Qing Zhao, Jing Liang, and Jun Chen (✉)

*Key Laboratory of Advanced Energy Materials Chemistry (Ministry of Education), Collaborative Innovation Center of Chemical Science and Engineering, College of Chemistry, Nankai University, Tianjin 300071, China*

**Received:** 23 July 2014
**Revised:** 15 September 2014
**Accepted:** 10 October 2014



**KEYWORDS**
graphene,
three-dimensional,
ice-template,
metal oxide,
sodium-ion battery

## ABSTRACT

We report on the ice-templated preparation and sodium storage of ultrasmall $SnO_2$ nanoparticles (3–4 nm) embedded in three-dimensional (3D) graphene ($SnO_2$@3DG). $SnO_2$@3DG was fabricated by hydrothermal assembly with ice-templated 3DG and a tin source. The structure and morphology analyses showed that 3DG has an interconnected porous architecture with a large pore volume of 0.578 $cm^3 \cdot g^{-1}$ and a high surface area of 470.5 $m^2 \cdot g^{-1}$. In comparison, $SnO_2$@3DG exhibited a pore volume of 0.321 $cm^3 \cdot g^{-1}$ and a surface area of 237.7 $m^2 \cdot g^{-1}$ with a homogeneous distribution of ultrasmall $SnO_2$ nanoparticles in a 3DG network. $SnO_2$@3DG showed a discharge capacity of 1,155 $mA \cdot h \cdot g^{-1}$ in the initial cycle, a reversible capacity of 432 $mA \cdot h \cdot g^{-1}$ after 200 cycles at 100 $mA \cdot g^{-1}$ (with capacity retention of 85.7% relative to that in the second cycle), and a discharge capacity of 210 $mA \cdot h \cdot g^{-1}$ at a high rate of 800 $mA \cdot g^{-1}$. This is due to the high distribution of $SnO_2$ nanoparticles in the 3DG network and the enhanced facilitation of electron/ion transport in the electrode.

## 1 Introduction

Three-dimensional graphene (3DG) has attracted much attention for its desirable physical and chemical properties such as low weight density, rich macroporosity and high electronic conductivity [1, 2]. To date, various methods including template-guided process, chemical vapor deposition (CVD) and solvothermal reactions have been devoted to the fabrication of 3DG [3, 4]. Ice-templating, which is also known as freeze drying, is a template-guided technique [5, 6]. So far, various types of 3D architecture graphene have been successfully synthesized by freeze drying. Mann and co-workers first prepared high-order 3D scaffolds by freeze casting of polystyrene sulfonate-stabilized graphene sheets and poly(vinyl alcohol) solution in liquid nitrogen [7]. Recently, 3D porous structure of graphene/cellulose composites were obtained on a large scale by ball milling and an ice-templated process [8]. It is found that assistant agents play an important

Address correspondence to chenabc@nankai.edu.cn

role as a linker to obtain 3D structure, but also cause troublesome purification. Thus, it is desirable to develop an additive-free approach. One of the critical issues when fabricating 3DG via ice-templated processes is the precursor, which should be highly stable [9]. Recently, a graphene colloid was synthesized by simply employing graphene oxide (GO) and $N_2H_4{\cdot}H_2O$ as the reactants in ammonia solution [10]. As the residual volatile $NH_3{\cdot}H_2O$ and $N_2H_4{\cdot}H_2O$ can be easily removed by evaporation, the colloidal graphene solution is a promising candidate precursor for the synthesis of 3D graphene.

To date, graphene-based composites have attracted tremendous interest for rechargeable batteries. For example, $SnO_2$/graphene is of interest in lithium ion batteries (LIBs) due to its high theoretical capacity (782 $mA{\cdot}h{\cdot}g^{-1}$ for $SnO_2$) and alleviation of particle aggregation as well as volume change during charge–discharge [11–14]. Moreover, $SnO_2$@3DG showed better lithium storage performance than that of $SnO_2$@2DG, which was attributed to the high surface area and 3D porous architecture [15]. Recently, $SnO_2$@2DG composites have been successfully applied in sodium-ion batteries (SIBs). For example, Wang's group prepared $SnO_2$/graphene composites with a stable capacity of 302 $mA{\cdot}h{\cdot}g^{-1}$ over 100 cycles at a current of 160 $mA{\cdot}g^{-1}$ [16], and Kim's group reported that the composites showed a reversible capacity of 330 $mA{\cdot}h{\cdot}g^{-1}$ over 150 cycles at 100 $mA{\cdot}g^{-1}$ [17]. This raises interesting questions about the electrochemical performance of $SnO_2$@3DG in SIBs?

In this work, $SnO_2$@3DG was successfully prepared and applied in SIBs. The preparation of 3DG involved a novel method using a graphene colloid and an ice-templated process. Furthermore, ice-templated 3DG turned out to be a robust substrate for anchoring $SnO_2$ via a simple hydrothermal treatment. The $SnO_2$@3DG displayed mesoporous character with a size distribution from 2 to 100 nm (centered at 3 nm and 30 nm), macropores (3–10 μm), large pore volume (0.321 $cm^3{\cdot}g^{-1}$) and high surface area (237.7 $m^2{\cdot}g^{-1}$). The $SnO_2$@3DG composites delivered a reversible capacity of 432 $mA{\cdot}h{\cdot}g^{-1}$ after 200 cycles at 100 $mA{\cdot}g^{-1}$ with a capacity retention of 85.7% (relative to that in the second cycle). Meanwhile, a reversible capacity of 210 $mA{\cdot}h{\cdot}g^{-1}$ was obtained at a high current density of 800 $mA{\cdot}g^{-1}$. This is a result of the high degree of distribution of $SnO_2$ nanoparticles in 3DG and the enhanced facilitation of electron/ion transport in the electrode.

## 2 Results and discussion

The four steps in the fabrication process of $SnO_2$@3DG are illustrated in Scheme 1. First, a graphene colloid was obtained by adding $NH_3{\cdot}H_2O$ and $N_2H_4{\cdot}H_2O$ to a GO aqueous suspension and the mixture heated at 95 ℃ for 1 h. Second, the extremely well-dispersed graphene solution was frozen at –18 ℃ to form an ice template with a subsequent lyophilization to obtain the reduced graphene oxide (rGO). Third, the 3DG was obtained by calcination at 350 ℃ for 2 h in an Ar atmosphere. During the thermal process, most of the residual water was removed, but the oxygenated functional groups were retained [18]. This results in an improvement in conductivity (Fig. S1, in the Electronic Supplementary Material (ESM)). Finally, a mixture of 3DG, $SnCl_2{\cdot}2H_2O$, and *N*,*N*-dimethylformamide was treated hydrothermally at 120 ℃ for 12 h to obtain $SnO_2$@3DG. For comparison, $SnO_2$@2DG was obtained in a similar way, except for the absence of a freeze-drying process.

Figures 1(a) and 1(b) show the scanning electron microscopy (SEM) images of 3DG. From Fig. 1(a), it can be seen that a highly interconnected 3D network is formed with various macropores. From Fig. 1(b), the cross-linked spots between 3DG can be seen, which

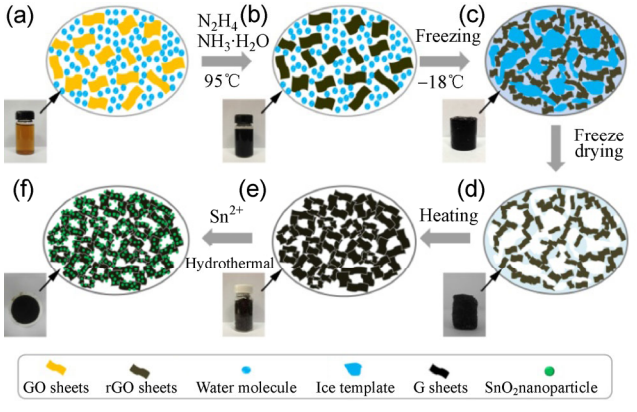


**Scheme 1** Schematic illustration of the preparation of $SnO_2$@3DG: (a) graphene oxide aqueous solution; (b) reduced graphene oxide colloid; (c) ice-templated solution; (d) reduced graphene oxide; (e) 3DG framework; (f) $SnO_2$@3DG composite.

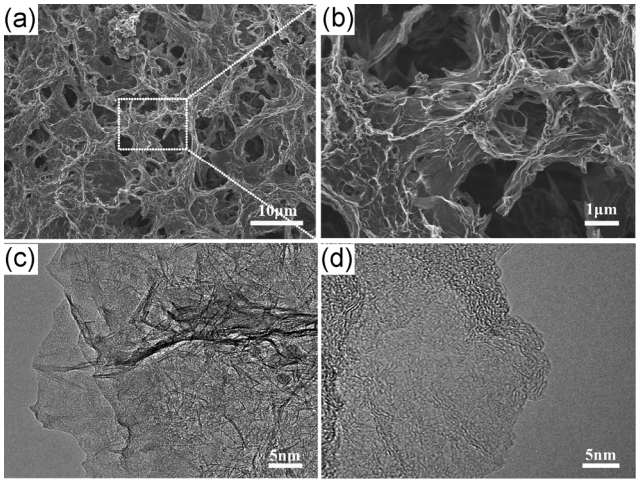


**Figure 1** (a) SEM image of 3DG; (b) magnified image of the selected region in (a); (c) TEM and (d) HRTEM images of 3DG.

stem from the partially stacked flexible graphene sheets. Figure 1(c) shows the transmission electron microscopy (TEM) image of graphene with few layers. Figure 1(d) shows the high-resolution TEM (HRTEM) image of the margin of the crumpled regions in 3DG. The above SEM and TEM images demonstrate the successful construction of 3DG. The successful synthesis is a result of several factors: (1) The reduction process gives partial removal of oxygenated groups such as hydroxyl and phenolic hydroxyl groups, but the carboxylic acid groups are still retained [19]. This leads to optimal electrostatic repulsion and the formation of a well-dispersed graphene colloid (Fig. S2, in the ESM). (2) In the colloidal dispersion, the large conjugated structure of graphene sheets can provide abundant π–π stacking sites and strong binding between the sheets. This induces the formation of cross-links through partial coalescence or overlap of graphene sheets. Simultaneously, the residual hydrophilic functionalities on the graphene sheets can entrap ample water molecules. (3) During the freezing process at –18 ˚C, the ice crystals formed act as a template, which leads to the formation of 3D networks after a sublimation process.

To gain a better understanding of the correlation between the graphene colloid and 3DG, a series of control experiments were performed using zeta potential analysis (Fig. S3, in the ESM). According to the standard for colloid stabilization, zeta potential values more negative than –30 mV are generally considered to present adequate repulsion to ensure the stability of colloids. Ammonia is found to be one of the key factors in obtaining the highly stable graphene colloid, since it can lead to the ionization of residual carboxylic acid moieties on the graphene. When the content of $NH_3{\cdot}H_2O$ reached to 750 μL (added to 100 mL of GO solution, 1 $mg{\cdot}mL^{-1}$), it gives the highest negative charge density on the graphene sheets (Fig. S3(a), in the ESM). $N_2H_4{\cdot}H_2O$ also has an effect on the zeta potential (Fig. S3(b), in the ESM). After further adding 60 μL of $N_2H_4{\cdot}H_2O$ to the above mixed solution, the graphene colloids shows a more negative charge density. As a consequence, 3DG can be obtained with 750 μL of $NH_3{\cdot}H_2O$ and 60 μL of $N_2H_4{\cdot}H_2O$ added to the GO solution. The successful formation of 3DG is ascribed to the residual moderately hydrophilic functionalities on the graphene, which can not only provide optimal electrostatic repulsion between the sheets, but also grasp ample water molecules to form the macroporous network. However, no 3D framework was obtained when $N_2H_4{\cdot}H_2O$ were added with the volumes of 30 μL or 90 μL (Figs. S3(c) and S3(d), in the ESM).

The 3DG has the following advantages as a support to embed $SnO_2$ nanoparticles: (1) The 3DG delivers a higher conductivity ($1.7 \times 10^{-1}$ $S{\cdot}cm^{-1}$) than that of graphene oxide ($3.4 \times 10^{-5}$ $S{\cdot}cm^{-1}$), which is attributed to its fewer number of functional groups; (2) There are more nucleation sites for $SnO_2$ on the GO than on rGO, which leads to more severe aggregation of $SnO_2$ particles (Fig. S4, in the ESM). Figure 2 shows the SEM and TEM images of $SnO_2$@3DG. The 3D structure of 3DG (Figs. 1(a) and 1(b)) is retained for $SnO_2$@3DG (Fig. 2(a)), without any significant breakdown. Uniform nanocrystals are homogeneously distributed on the graphene sheets (Fig. 2(b)). The TEM image in Fig. 2(c) further illustrates that $SnO_2$ nanoparticles with an average particle size of 3.4 nm (inset of Fig. 2(c)) are homogeneously dispersed on graphene sheets. Moreover, tremendous nano-lacunas are formed among the nanoparticles. This is favorable in terms of tolerating the large volume expansion during the charge–discharge process [20]. The HRTEM image in Fig. 2(d) reveals a crystal lattice spacing of 0.33 nm, corresponding to the interplanar spacing of the (110) planes of $SnO_2$. The selected-area-electron diffraction

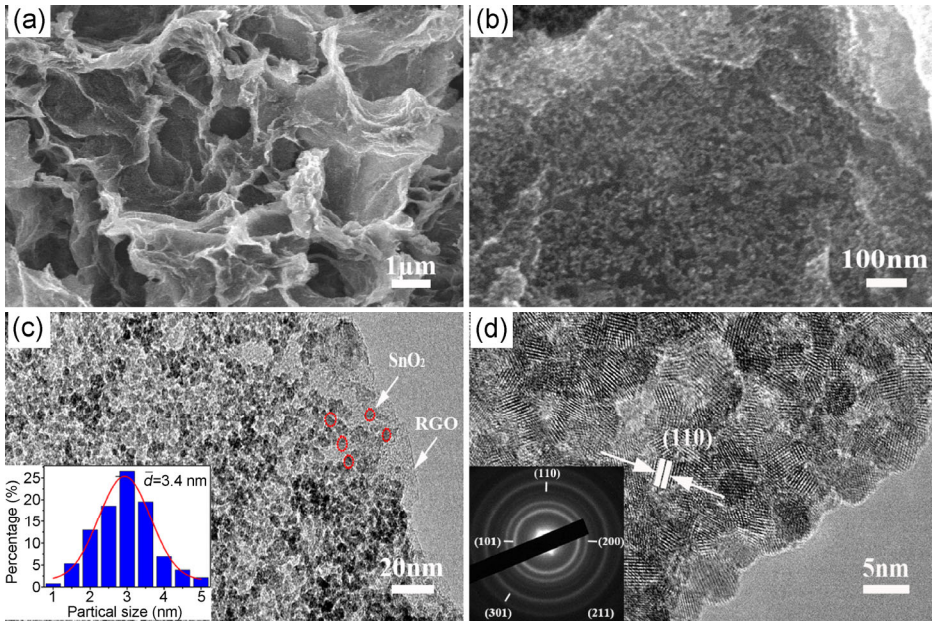


**Figure 2** (a) and (b) SEM images of $SnO_2$@3DG; (c) TEM image of $SnO_2$@3DG. Inset: The corresponding particle size distribution diagram with the calculation of 100 particles; (d) HRTEM image of $SnO_2$@3DG. Inset: The corresponding SAED pattern.

(SAED) pattern (inset of Fig. 2(d)) confirms the presence of polycrystalline $SnO_2$ nanoparticles. In comparison, $SnO_2$@2DG shows a typical sheet-like 2D structure, in which ultrasmall $SnO_2$ nanocrystals (3–5 nm) are anchored on the surface of graphene (Figs. S5(a)–S5(c), in the ESM).

The crystal phases of 3DG, $SnO_2$@2DG, and $SnO_2$@3DG were analyzed by X-ray diffraction (XRD), as shown in Fig. 3(a). The XRD pattern of 3DG clearly reveals the typical characteristic of graphene with a hump at 24°–28°. The XRD patterns of both $SnO_2$@3DG and $SnO_2$@2DG exhibit similar diffraction peaks that can be readily indexed to tetragonal rutile $SnO_2$ (JCPDS No. 41-1445). However, no diffraction peaks of graphene could be found in the XRD patterns of either composite, which could be explained by the fact that the strong signals of $SnO_2$ obscure the characteristic peaks of graphene sheets. Figure 3(b) shows the Raman spectra of the three samples, in which two broad peaks at 1,335 $cm^{-1}$ (D band) and 1,593 $cm^{-1}$ (G band) are typical characteristics of graphene. Moreover, X-ray photoelectron spectroscopy (XPS) was employed to explore the nature of the interaction between $SnO_2$ and graphene (Fig. S6, in the ESM). The scan spectra up to binding energy of 1,200 eV (Fig. S6(a)) display the presence of C, O and Sn elements. The spectrum in the binding energy range of 480 to 500 eV (Fig. S6(b)) shows the peaks of Sn $3d_{3/2}$ and Sn $3d_{5/2}$, indicating the formation of $SnO_2$-containing composites. The C 1s spectra of the composites are shown in Fig. S6(c). The peak at 284.8 eV is assigned to C–C, while the peak at 286.6 eV corresponds to C–O–Sn. This indicates the formation of C–O–Sn bonds between the $SnO_2$ and graphene [21].

The $SnO_2$ contents in both composites were measured by thermogravimetric analysis (TGA). As shown in Fig. 3(c), the weight percentages of $SnO_2$ in $SnO_2$@3DG and $SnO_2$@2DG are 71.5% and 70.4%, respectively. In addition, the content of $SnO_2$ in $SnO_2$@3DG has an obvious effect on the 3D structure. A 3D structure with many large pores is obtained with a lower loading mass of $SnO_2$ (40.2%) in the composite (Fig. S7(a), in the ESM). Figures S7(b)–S7(d) show that the 3D structure gradually changes as the content of $SnO_2$ increases. When the mass loading of $SnO_2$ is 90.5%, the 3D structure in the composite completely collapses. Figure 3(d) shows that the Brunauer–Emmett–Teller (BET) surface area of 3DG is as high as 470.5 $m^2 \cdot g^{-1}$. Moreover, the specific surface area of $SnO_2$@3DG (237.7 $m^2 \cdot g^{-1}$) is about twice that of $SnO_2$@2DG (113.5 $m^2 \cdot g^{-1}$). This result highlights that the ice-templated strategy is an effective way to obtain a high

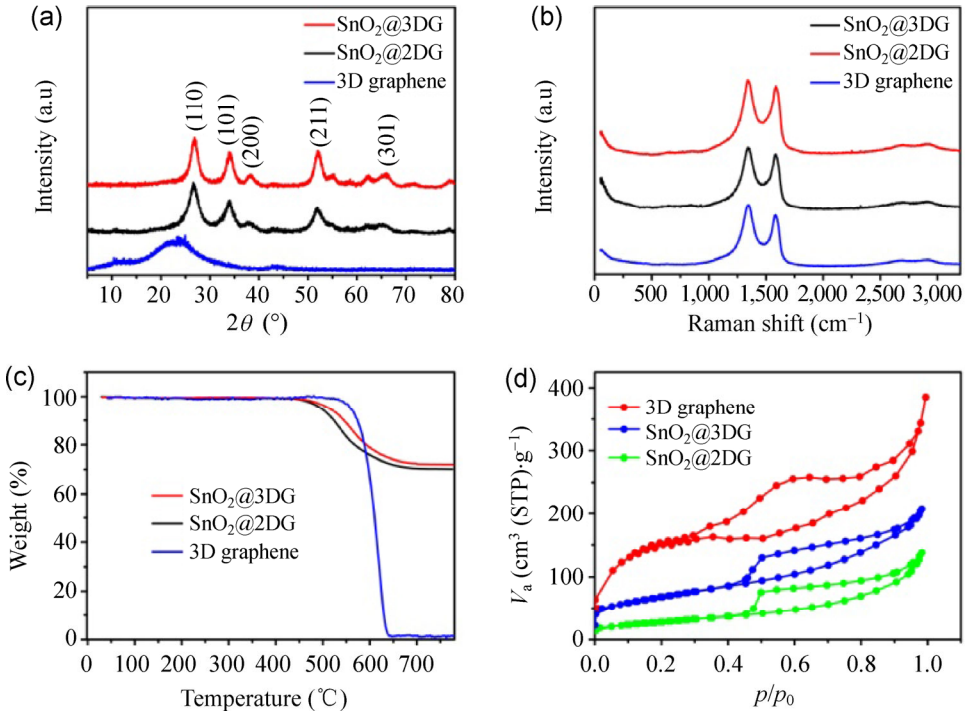


**Figure 3** (a) XRD profiles, (b) Raman spectra, (c) TGA curves, and (d) $N_2$ adsorption–desorption isotherms of $SnO_2$@3DG (71.5% $SnO_2$), $SnO_2$@2DG (70.4% $SnO_2$) and 3DG.

surface area. Based on the Barrett–Joyner–Halenda method, the maxima in the pore size distribution of $SnO_2$@3DG occur at around 3 nm and 30 nm (Fig. S8, in the ESM). The broad pore size distribution spanning from 2 to 100 nm implies that $SnO_2$@3DG is rich in hierarchical pores. Consequently, the high surface area and rich porosity of $SnO_2$@3DG are closely related to the presence of meso/macro pores.

The sodium storage performance of $SnO_2$@3DG and $SnO_2$@2DG was investigated. Figures 4(a) and 4(b) show the charge–discharge curves of $SnO_2$@3DG and $SnO_2$@2DG tested at a current density of 100 mA·g$^{-1}$. The $SnO_2$@3DG electrode exhibits a high discharge capacity of 1,155 mA·h·g$^{-1}$ and a charge capacity of 480 mA·h·g$^{-1}$ in the initial cycle (inset of Fig. 4(a)). The irreversible capacity loss (675 mA·h·g$^{-1}$) mainly originated from the formation of a solid electrolyte interphase (SEI) film [16, 17, 22], while the side reaction of oxygen-containing functional groups on graphene also leads to partial capacity loss (ca. 70 mA·h·g$^{-1}$, Fig. S9 (in the ESM)). During the second cycle, it delivers a discharge capacity of 504 mA·h·g$^{-1}$, accounting for 94.4% of the theoretical capacity (533.9 mA·h·g$^{-1}$, Fig. S10 (in the ESM)). This indicates a high utilization of the active material in the composite. Notably, a reversible capacity of 432 mA·h·g$^{-1}$ is still maintained after 200 cycles. In contrast, the $SnO_2$@2DG electrode exhibits a discharge capacity of 1,067 mA·h·g$^{-1}$ and a charge capacity of 411 mA·h·g$^{-1}$ (inset of Fig. 4(b)). The capacity retention is 78.9% and the maintained capacity after 200 cycles is only 301 mA·h·g$^{-1}$. Figure 4(c) shows the rate performance of the two composites. $SnO_2$@3DG delivers capacities of 551 mA·h·g$^{-1}$ and 210 mA·h·g$^{-1}$ at 50 and 800 mA·g$^{-1}$, respectively. However, $SnO_2$@2DG shows capacities of only 391 mA·h·g$^{-1}$ and 127 mA·h·g$^{-1}$ at 50 and 800 mA·g$^{-1}$, respectively. Figure 4(d) exhibits the cycling performance of the composites. The $SnO_2$@3DG electrode shows an obviously enhanced cycling performance compared to that of $SnO_2$@2DG. The $SnO_2$@3DG electrode retains a reversible capacity of 432 mA·h·g$^{-1}$ after 200 cycles (85.7% capacity retention relative to the second cycle). This result is superior to that of $SnO_2$@2DG (301 mA·h·g$^{-1}$ after 200 cycles, 71.4% capacity retention) and those reported for $SnO_2$/graphene materials [16, 17]. To investigate the effect of the unique structure on the cycling performance, $SnO_2$@3DG composites with different contents of $SnO_2$ are

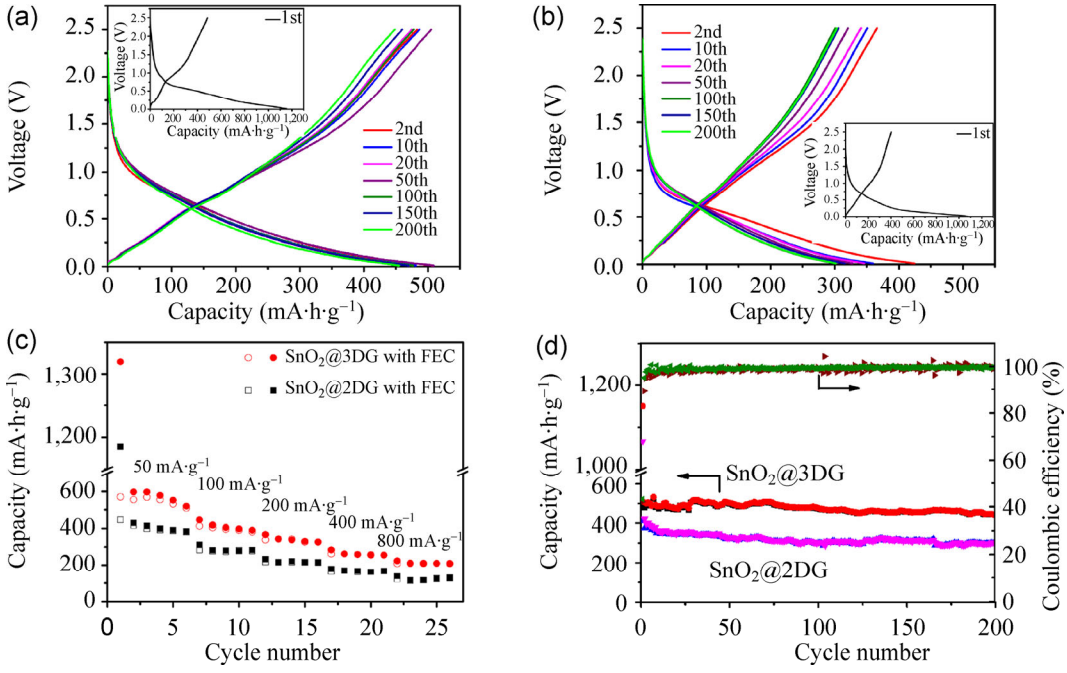


**Figure 4** Charge–discharge curves of (a) $SnO_2$@3DG (71.5% $SnO_2$) and (b) $SnO_2$@2DG (70.4% $SnO_2$) at a current density of 100 mA·g$^{-1}$; (c) rate performance of $SnO_2$@3DG and $SnO_2$@2DG tested at different current densities from 50 to 800 mA·g$^{-1}$; (d) Cycling performance of $SnO_2$@3DG and $SnO_2$@2DG at the current density of 100 mA·g$^{-1}$.

compared (Fig. S11, in the ESM). The composites with low mass loadings of $SnO_2$ (40.2% and 57.4%) deliver relatively low capacity but show good cycling performance. In contrast, the composite with a much higher mass loading of $SnO_2$ (90.5%) shows an initial high capacity but with inferior cycling stability, which can be ascribed to the severe aggregation and pulverization of nanoparticles (Fig. S12, in the ESM). The 3D framework limits the agglomeration and pulverization of $SnO_2$ nanoparticles during the sodiation/desodiation process, which is mostly responsible for the enhanced capacity and high-rate cycling performance. Thus the $SnO_2$@3DG composite with a $SnO_2$ mass loading of 71.5% shows the optimum combination of high capacity and stable cycling.

Figures 5(a) and 5(b) show the Nyquist plots of $SnO_2$@3DG and $SnO_2$@2DG. The high frequency semicircle is associated with sodium-ion migration through the SEI film and the middle frequency semicircle is linked to the charge transfer reaction. The charge transfer resistance ($R_{ct}$) values of $SnO_2$@3DG decreases from 48.5 Ω at 308 K to 32.2 Ω at 328 K, while the $SnO_2$@2DG shows $R_{ct}$ values of 77.3 Ω at 308 K and 35.9 Ω at 328 K. This indicates that in the measured temperature range, higher temperature results in better electrode kinetics. Both composites show similar $R_e$ values while the $R_{SEI}$ values of $SnO_2$@3DG are higher than those of $SnO_2$@2DG, which is due to the larger surface area of $SnO_2$@3DG (Table S1, in the ESM). The exchange currents ($i_0$) and the apparent activation energies ($E_a$) for the intercalation of sodium are calculated by the following equations [23]:

$$i_0 = RT/nFR_{ct} \quad (1)$$

$$i_0 = A\exp(-E_a/RT) \quad (2)$$

The calculated value of $E_a$ is 20.2 kJ·mol$^{-1}$ for $SnO_2$@3DG and 35.8 kJ·mol$^{-1}$ for $SnO_2$@2DG (Fig. 5(c), and Eq. (S1) in the ESM). The lower activation energy of $SnO_2$@3DG is indicative of more facile sodium intercalation kinetics [24, 25]. The enhanced kinetics arises from the particular structure of the $SnO_2$@3DG composites, in which the 3D graphene architecture can not only provide a high electronic and ionic conductivity but also offer large surface areas that favor effective contact between electrolyte and materials.

An explanation of the much better electrochemical performance of $SnO_2$@3DG compared with that of

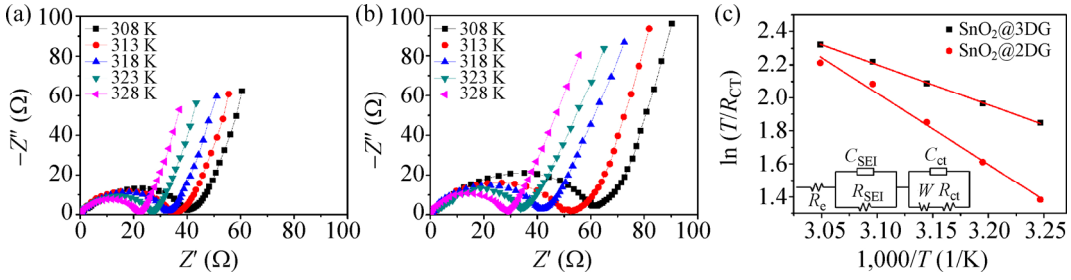


**Figure 5** Electrochemical impedance spectra (EIS) plots of (a) $SnO_2$@3DG (71.5% $SnO_2$) and (b) $SnO_2$@2DG (70.4% $SnO_2$) from 308 K to 328 K with 50% depth of discharge in the second cycle; (c) Arrhenius plots of $\ln(T/R_{ct})$ versus $1/T$. Inset: the equivalent circuits of $SnO_2$@3DG and $SnO_2$@2DG. $R_e$ is electrolyte resistance. $R_{SEI}$ and $C_{SEI}$ are the resistance and constant phase element of SEI film. $R_{ct}$ and $C_{ct}$ represent the charge transfer resistance and a constant phase element, respectively. $W$ is the Warburg impendence related to the diffusion of sodium ions.

$SnO_2$@2DG is schematically shown in Scheme 2. The elastic and specific 3D structures can not only enhance the mechanical strength of electrodes, but also act as a buffer that accommodates the volume expansion of $SnO_2$ nanocrystals during the charge–discharge process. Second, the large surface area and various meso-/macro pores of $SnO_2$@3DG can offer multidimensional channels to facilitate the transport of $Na^+$ in the electrode. This should shorten the diffusion length from the external electrolyte to the interior surface and afford easy electrolyte accessibility.

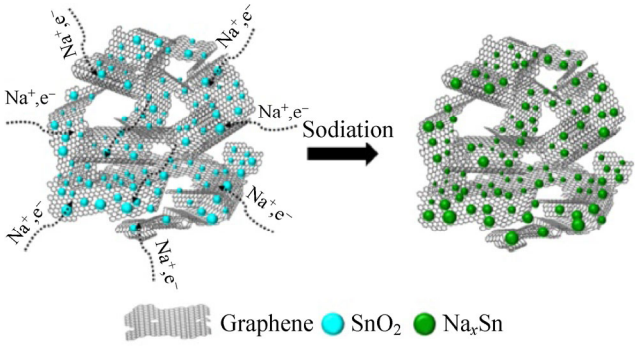


**Scheme 2** Schematic illustration of the efficacy of $SnO_2$@3DG for sodium storage during the charge–discharge process.

## 3 Conclusions

$SnO_2$@3DG has been successfully prepared by assembling ice-templated 3DG with a tin source in a hydrothermal process and employed in SIBs. The as-prepared $SnO_2$@3DG shows a hierarchical porous architecture with meso/macro-pores and large surface area. Moreover, it exhibits a high cycling stability and a high rate performance. A reversible capacity of 432 mA·h·g$^{-1}$ and high capacity retention of 85.7% were maintained over 200 cycles at 100 mA·g$^{-1}$. Even at a high current density of 800 mA·g$^{-1}$, the capacity was 210 mA·h·g$^{-1}$. The enhanced performance can be attributed to the effective limitation of agglomeration and pulverization of $SnO_2$ nanoparticles during the sodiation/desodiation process by the 3D network, and the high electronic and ionic conductivity of 3DG.

## 4 Experimental methods

### *4.1.1 Synthesis of graphene solution with different volumes of $NH_3·H_2O$*

Graphene oxide was prepared from graphite (325 mesh, Alfa Aesar) by a modified Staudenmeier method [26]. The obtained GO (100 mg) was dispersed in distilled water (100 mL) and then exfoliated to generate GO nanosheets by ultrasonication. The brown suspension was transferred to a round-bottomed flask, to which different amounts of $NH_3·H_2O$ (0, 250, 500, 750, 1,000, 1,250, 1,500, 1,750, 2,000 μL) were added. Finally, the solution was stirring in an oil bath at 95 ℃ for 1 h.

### *4.1.2 Synthesis of graphene colloid with different volumes of $N_2H_4·H_2O$*

100 mg of GO was dispersed in distilled water (100 mL) and then exfoliated to generate GO nanosheets by ultrasonication. The brown suspension was transferred to a round-bottomed flask and 750 μL of $NH_3·H_2O$ was added to the mixture. Subsequently, different amounts of $N_2H_4·H_2O$ (80%, Guangfu Fine Chemicals, Tianjin, China), namely 0, 30, 60, 90, 120, 150, 180, 210, and 240 μL were added. The solution was stirred in

an oil bath at 95 ℃ for 1 h. After cooling naturally, the solution was frozen at –18 ℃ in the refrigerator and directly dehydrated via a freeze drying process to maintain the 3D monolithic architecture. Finally, the as-prepared 3DG was treated by calcination at 350 ℃ for 2 h in Ar.

#### 4.1.3 *Synthesis of $SnO_2$@3DG*

In a typical procedure, 80 mg of 3D graphene was dispersed in a mixture of 80 mL of *N*,*N*-dimethylformamide (DMF) and 10 mL of deionized water. Subsequently, a precise amount of $SnCl_2{\cdot}2H_2O$ (0.4 g, Guangfu Fine Chemicals, Tianjin, China) were added to the solution followed by adding 1 mL of HCl (36.0%–38.0%). After stirring for 5 h, the suspension was transferred to a Teflon-lined autoclave (100 mL in capacity), sealed tightly, and heated at 120 ℃ for 12 h. The obtained $SnO_2$@3DG was washed several times with ethanol and dried under vacuum at 120 ℃ for 24 h.

#### 4.1.4 *Synthesis of $SnO_2$@2DG*

The preparation of $SnO_2$@2DG was similar to the process for $SnO_2$@3DG, except for the replacement of 3DG with 2DG. The 2DG was synthesized by adding $NH_3{\cdot}H_2O$ (750 μL) and $N_2H_4{\cdot}H_2O$ (60 μL) to a GO solution (100 mg, 1 mg/mL) without freeze drying, but using a direct filtration and drying process in a vacuum oven.

### 4.2 Materials characterization

Structural analysis was carried out by powder X-ray diffraction (XRD, Rigaku MiniFlex600, Cu K$\alpha$ radiation) with a scanning speed of 4(°)·min$^{-1}$ from 10°–80°. Raman spectra were obtained using a confocal Raman microscope (DXR, Thermo Fisher Scientific) at 532 nm excitation from an argon-ion laser. Morphologies and structures were characterized by SEM (FEI Nanosem 430, 10 kV) and TEM (Philips Tecnai G2F20, 200 kV). The specific surface area and pore size distribution were analyzed using Brunauer–Emmett–Teller (BET) nitrogen adsorption/desorption isotherms at 77 K on a BELSORP-mini instrument. The TGA measurements were carried out in air flow at a heating rate of 5 ℃·min$^{-1}$ using a Netzsch STA 449 F3 Jupiter analyzer. The zeta potentials were measured with Zetasizer (Malvern, Nano ZS90). The Fourier transform infrared (FT-IR) spectra were recorded on a FTIR-650 spectrometer (Gangdong Co., Ltd., Tianjin, China).

The working electrodes were prepared by dispersing the as-prepared material, carbon black, and poly(vinylidene fluoride) binder in a weight ratio of 8:1:1. The resulting slurry was pasted onto copper foil and dried at 110 ℃ in vacuum for 8 h. By using Na as counter and reference electrodes, and glass microfiber (Whatman) as the separator, CR2032-type coin cells were assembled in an argon-filled glove box (Mikrouna Universal 2440/750). The electrolyte was 1 M $NaClO_4$ in tetraethylene glycol dimethyl ether (TEGDME) with 5 wt.% fluoroethylene carbonate (FEC). The assembled cells were tested at different rates in the voltage range 0.01 to 2.5 V using a LAND-CT2001A battery-testing instrument. EIS were collected with an AC voltage of 5 mV amplitude in the frequency range from 100 kHz to 10 mHz.

## Acknowledgements

This work was supported by the National Basic Research Program of China (973 Programs) (No. 2011CB935900), the National Natural Science Foundation (NSFC) (No. 51231003), Ministry of Education of the People's Republic of China (No. IRT13R30 and B12015), and Tianjin High-Tech (No. 13JCQNJC06400 and 12ZCZDJC35300).

**Electronic Supplementary Material**: Supplementary material (colloid tests, FT-IR spectra, SEM images and zeta potential of 3DG prepared with different amounts of $NH_3{\cdot}H_2O$ and $N_2H_4{\cdot}H_2O$, SEM images and TEM images of $SnO_2$@2DG, SEM images and electrochemical performances of $SnO_2$@3DG with different $SnO_2$ contents, pore size distribution of $SnO_2$@3DG, and $R_{ct}$ values of $SnO_2$@3DG and $SnO_2$@2DG) is available in the online version of this article at http://dx.doi.org/10.1007/s12274-014-0609-6.

## Reference

[1] Huang, X.; Qi, X. Y.; Boey, F.; Zhang, H. Graphene-based composites. *Chem. Soc. Rev.* **2012**, *41*, 666–686.

[2] Xu, Y. X.; Huang, X. Q.; Lin, Z. Y.; Zhong, X.; Huang, Y.; Duan, X. F. One-step strategy to graphene/Ni(OH)$_2$ composite hydrogels as advanced three-dimensional supercapacitor electrode materials. *Nano Res.* **2013**, *6*, 65–76.

[3] Li, C.; Shi, G. Q. Three-dimensional graphene architectures. *Nanoscale* **2012**, *4*, 5549–5563.

[4] Nardecchia, S.; Carriazo, D.; Luisa Ferrer, M.; Gutierrez, M. C.; del Monte, F. Three dimensional macroporous architectures and aerogels built of carbon nanotubes and/or graphene: Synthesis and applications. *Chem. Soc. Rev.* **2013**, *42*, 794–830.

[5] Li, W. L.; Lu, K.; Walz, J. Y. Freeze casting of porous materials: review of critical factors in microstructure evolution. *Inter. Mater. Rev.* **2012**, *57*, 37–60.

[6] Xu, Y. X.; Sheng, K. X.; Li, C.; Shi, G. Q. Self-assembled graphene hydrogel via a one-step hydrothermal process. *ACS Nano* **2010**, *4*, 4324–4330.

[7] Vickery, J. L.; Patil, A. J.; Mann, S. Fabrication of graphene–polymer nanocomposites with higher-order three-dimensional architectures. *Adv. Mater.* **2009**, *21*, 2180–2184.

[8] Ouyang, W. Z.; Sun, J. H.; Memon, J.; Wang, C.; Geng, J. X.; Huang, Y. Scalable preparation of three-dimensional porous structures of reduced graphene oxide/cellulose composites and their application in supercapacitors. *Carbon* **2013**, *62*, 501–509.

[9] Deville, S. Freeze-casting of porous ceramics: A review of current achievements and issues. *Adv. Energy Mater.* **2008**, *10*, 155–169.

[10] Li, D.; Müller, M. B.; Gilje, S.; Kaner, R. B.; Wallace, G. G. Processable aqueous dispersions of graphene nanosheets. *Nat. Nanotechnol.* **2008**, *3*, 101–105.

[11] Chen, S.; Wang, M.; Ye, J. F.; Cai, J. G.; Ma, Y. R.; Zhou, H. H.; Qi, L. M. Kinetics-controlled growth of aligned mesocrystalline $SnO_2$ nanorod arrays for lithium-ion batteries with superior rate performance. *Nano Res.* **2013**, *6*, 243–252.

[12] Zhou, X.; Wan, L.-J.; Guo, Y.-G. Binding $SnO_2$ nanocrystals in nitrogen-doped graphene sheets as anode materials for lithium-ion batteries. *Adv. Mater.* **2013**, *25*, 2152–2157.

[13] Kim, H.; Kim, S.-W.; Park, Y.-U.; Gwon, H.; Seo, D.-H.; Kim, Y.; Kang, K. $SnO_2$/graphene composite with high lithium storage capability for lithium rechargeable batteries. *Nano Res.* **2010**, *3*, 813–821.

[14] Cui, L. F.; Shen, J.; Cheng, F. Y.; Tao, Z. L.; Chen, J. $SnO_2$ nanoparticles@polypyrrole nanowires composite as anode materials for rechargeable lithium-ion batteries. *J. Power Sources* **2011**, *196*, 2195–2201.

[15] Huang, Y. S.; Wu, D. Q.; Han, S.; Li, S.; Xiao, L.; Zhang, F.; Feng, X. L. Assembly of tin oxide/graphene nanosheets into 3D hierarchical frameworks for high-performance lithium storage. *ChemSusChem* **2013**, *6*, 1510–1515.

[16] Su, D. W.; Ahn, H.-J.; Wang, G. X. $SnO_2$@graphene nanocomposites as anode materials for Na-ion batteries with superior electrochemical performance. *Chem. Commun.* **2013**, *49*, 3131–3133.

[17] Wang, Y.-X.; Lim, Y.-G.; Park, M.-S.; Chou, S.-L.; Kim, J. H.; Liu, H.-K.; Dou, S.-X.; Kim, Y.-J. Ultrafine $SnO_2$ nanoparticle loading onto reduced graphene oxide as anodes for sodium-ion batteries with superior rate and cycling performances. *J. Mater. Chem. A* **2014**, *2*, 529–534.

[18] Xiao, M.; Du, X. S.; Meng, Y. Z.; Gong, K. C. The influence of thermal treatment conditions on the structures and electrical conductivities of graphite oxide. *New Carbon Mater.* **2004**, *19*, 92–96.

[19] Nguyen, S. T.; Ruoff, R. S.; Stankovich, S.; Dikin, D. A.; Piner, R. D.; Kohlhaas, K. A.; Kleinhammes, A.; Jia, Y.; Wu, Y. Synthesis of graphene-based nanosheets via chemical reduction of exfoliated graphite oxide. *Carbon* **2007**, *45*, 1558–1565.

[20] Zhu, Z. Q.; Cheng, F. Y.; Chen, J. Investigation of effects of carbon coating on the electrochemical performance of $Li_4Ti_5O_{12}$/C nanocomposites. *J. Mater. Chem. A* **2013**, *1*, 9484–9490.

[21] Liang, J. F.; Cai, Z.; Tian, Y.; Li, L. D.; Geng, J. X.; Guo, L. Deposition $SnO_2$/nitrogen-doped graphene nanocomposites on the separator: A new type of flexible electrode for energy storage devices. *ACS Appl. Mater. Inter* **2013**, *5*, 12148–12155.

[22] Wang, Z. Y.; Zhang, H.; Li, N.; Shi, Z. J.; Gu, Z. N.; Cao, G. P. Laterally confined graphene nanosheets and graphene/$SnO_2$ composites as high-rate anode materials for lithium-ion batteries. *Nano Res.* **2010**, *3*, 748–756.

[23] Wang, L. J.; Zhang, K.; Hu, Z.; Duan, W. C.; Cheng, F. Y.; Chen, J. Porous CuO nanowires as the anode of rechargeable Na-ion batteries. *Nano Res.* **2014**, *7*, 199–208.

[24] Cheng, F. Y.; Wang, H. B.; Zhu, Z. Q.; Wang, Y.; Zhang, T. R.; Tao, Z. L.; Chen, J. Porous $LiMn_2O_4$ nanorods with durable high-rate capability for rechargeable Li-ion batteries. *Energ Environ. Sci.* **2011**, *4*, 3668–3675.

[25] Gao, H.; Hu, Z.; Zhang, K.; Cheng, F.; Chen, J. Intergrown $Li_2FeSiO_4$·$LiFePO_4$–C nanocomposites as high-capacity cathode materials for lithium-ion batteries. *Chem. Commun.* **2013**, *49*, 3040–3042.

[26] McAllister, M. J.; Li, J.-L.; Adamson, D. H.; Schniepp, H. C.; Abdala, A. A.; Liu, J.; Herrera-Alonso, M.; Milius, D. L.; Car, R.; Prud'homme, R. K.; et al. Single sheet functionalized graphene by oxidation and thermal expansion of graphite. *Chem. Mater.* **2007**, *19*, 4396–4404.